nature communications

Article | Article in Press

https://doi.org/10.1038/s41467-026-77786-5

Disentangling the effect of space and electric field on photoelectrochemical water splitting

Received: 30 March 2026

Accepted: 3 September 2026

Published online: 12 September 2026

Check for updates

Dongfeng Li[1], Lingcong Zhang[2,3], Yanjun Xu[1,4], Longjie Wang[2,4], Hanting Meng[1,4], Yin Huang[1], Jiading Zou[1,5], Zhuan Wang[1,5], Hailong Chen[1,4,5], Li Liu[1] ✉, Xiuli Wang[2] ✉ & Yuxiang Weng[1,4,5] ✉

Photoelectrochemical water splitting is a promising pathway for renewable solar fuel production. The photoelectrochemical performance strongly depends on the charge separation ability within the space charge layer. In space charge layer, the charge dynamics should be governed by band bending profile consisting with built-in electric field and space charge layer width, yet the precise mechanisms remain unclear. Herein, using Sn doping to regulate band bending profile of Fe_2O_3 photoanode, we disentangle the effect of space charge layer width and built-in electric field on charge dynamics in photoelectrochemical water splitting by in-situ time-resolved spectroscopies. Space charge layer width determines the onset of photogenerated charge separation, exhibiting a threshold of ~2.4 nm. Above W_{SCL} threshold, the strong built-in electric field in Fe_2O_3 photoanode effectively empties the occupied electron trap states and blocks the recombination between the back electrons and charged intermediates, thereby facilitating surface hole accumulation for improving water oxidation reaction rate.

Photoelectrochemical (PEC) water splitting using a semiconductor photoelectrode is a promising pathway for producing clean solar fuel[1–4]. The solar-to-chemical conversion efficiency of a photoelectrode depends on the effective separation of photoinduced charge, which is determined by the band bending profile in the space charge layer[5]. Although the importance of band bending profile in charge separation has been widely demonstrated, its specific mechanism on charge dynamics remains unclear, and need to be comprehensively understood.

In the band bending profile, the built-in potential (V_{bi}) and the space charge layer width (W_{SCL}) jointly determine the magnitude of the built-in electric field (E_{bi}), which is the driving force for charge separation[5,6]. Generally, the larger E_{bi} is regarded as having a higher charge separation capability. For example, the anisotropic photogenerated charge separation on different facets of a $BiVO_4$ or Cu_2O photocatalyst is attributed to the distinct E_{bi}, which is derived by the surface photovoltage microscopy[7,8]. Since the W_{SCL} in the band bending profile determines the amount of photogenerated charges, the wider W_{SCL} should contribute to the higher charge separation capability. Barroso et al. assigned the cathodic shift of long-lived photo-hole signal in surface-modified Fe_2O_3 photoanode to the enhancement of W_{SCL}[9]. In the photoanode system, both E_{bi} and W_{SCL} are increased with the applied potential, thereby generating higher photocurrent[10–12]. Moreover, the in-situ time-resolved spectroscopies directly monitor the extension of lifetime for photogenerated charge with the potential increase[12–17]. Si-[13] or Ti-doped[17] Fe_2O_3 photoanodes exhibit stronger bleach intensity (electron signal) and longer decay lifetime (hole signal) with increasing the applied potentials. On the other hand, researchers claimed that the alteration of the E_{bi} and W_{SCL} induces no detectable perturbation to photogenerated charge

[1]Laboratory of Soft Matter Physics, Beijing National Laboratory for Condensed Matter Physics, Institute of Physics, Chinese Academy of Sciences, Beijing 100190, China. [2]State Key Laboratory of Catalysis, Dalian Institute of Chemical Physics, Chinese Academy of Sciences, Dalian National Laboratory for Clean Energy, Dalian 116023, China. [3]School of Materials Science and Engineering and National Institute for Advanced Materials, Nankai University, Tianjin 300350, China. [4]University of Chinese Academy of Sciences, Beijing 100049, China. [5]Songshan Lake Materials Laboratory, Dongguan 523808 Guangdong, China. ✉e-mail: li.liu@iphy.ac.cn; xiuliwang@dicp.ac.cn; yxweng@iphy.ac.cn

dynamics[17–20]. With an increase in E_{bi} and W_{SCL} through the applied potential, there is no significant spectral change on the undoped Fe_2O_3 photoanode[17,18]. Obviously, the Fe_2O_3-based photoanodes exhibit two different characteristics under the changed E_{bi} and W_{SCL}. Although both E_{bi} and W_{SCL} serve as the descriptors for charge separation capability, the mutual modulation between these parameters, in conjunction with other side effects (the shift of energy band edge[21], or introduction of mid-gap impurity states[22]), complicates the underlying mechanisms. Therefore, understanding the individual contribution of E_{bi} and W_{SCL} to charge dynamics is vital, but remains lacking.

Herein, taking Fe_2O_3-based photoanodes as a model, we studied the role of band bending profile in photoinduced charge dynamics. The band bending profiles of Fe_2O_3 were regulated by doping the Sn element into Fe_2O_3 (Sn-Fe_2O_3). The functions of W_{SCL} and E_{bi} on the PEC performances and back electron recombination were studied. The influence of W_{SCL} and E_{bi} on in-situ charge dynamics on fs-s timescale was disentangled in water oxidation reaction. The WSCL determines the onset of the photocurrent of the oxygen evolution reaction (OER), and the E_{bi} blocks the back electron recombination. The mechanism study advances the fundamental understanding of the band bending profile in photo(electro)catalysis, and provides a direction for promoting photo(electro)catalytic efficiency.

Results and discussion

Modulation of band bending profile of Fe_2O_3 photoanode through Sn doping

Since the W_{SCL} is influenced by the carrier density N_d ($W_{SCL} \propto N_d^{0.5}$, Methods), Fe_2O_3 photoanodes with/without Sn doping were chosen to modulate the band bending profile of Fe_2O_3 photoanode, which were prepared by a combined method of hydrothermal and high-temperature calcination[16]. The Fe_2O_3 photoanodes are n-type demonstrated by the positive slopes in Mott-Schottky curves in Fig. 1a. The Sn-Fe_2O_3 photoanode shows a smaller slope corresponding to higher density of majority carrier N_d ($2.6 \times 10^{20}\,cm^{-3}$) than the pristine Fe_2O_3 photoanode ($1.2 \times 10^{20}\,cm^{-3}$) (the calculated details are in Methods). Importantly, the two photoanodes display the same flat band potential V_{fb} at 0.34 V_{RHE}, indicating the same built-in potential from surface to bulk with the same applied potential. These two Fe_2O_3 photoanodes provide the possibility to construct different band bending profiles with equivalent built-in potentials at a given applied potential, thereby disentangling the influence of E_{bi} and W_{SCL} factors. By plotting the W_{SCL} with applied potentials (Fig. 1b), the Sn-Fe_2O_3 photoanode displays narrower W_{SCL} than the pristine Fe_2O_3 photoanode, and the W_{SCL} (0 ~ 7 nm) are consistent with the reported W_{SCL} values[23]. Moreover, by comparing experiment (Mott-Schottky analysis) and calculation (density functional theory), Delcompare-Rodriguez et al. has verified the validation of W_{SCL} regions on the order of only a few nanometers in hematite[24]. The narrower W_{SCL} in Sn-Fe_2O_3 photoanode causes faster reduction of E_{bi} from surface to bulk (Fig S1a), resulting in larger E_{bi} at the photoanode surface (Fig. 1c). As shown in Fig. 1c, Sn-Fe_2O_3 photoanode surface at 0.97 V_{RHE} produces a strong E_{bi} of 0.43 V nm^{-1}, whereas the pristine Fe_2O_3 photoanode requires a high potential of 1.7 V_{RHE} to achieve this E_{bi}. In addition, the Sn-Fe_2O_3 photoanode displays similar density of surface trap states and bulk charge transport rate to pristine Fe_2O_3 (Figs. S2–S7), implying that Sn doping does not bring more defects, and change conductivity. In Figure S8-S9, the similar surface morphology, crystal structure, and light absorption for two films further demonstrate the mild influence of surface Sn doping on Fe_2O_3 properties. Comparing the photocurrents of two photoanodes in water and sulfite oxidation (Fig. S10), the surface state-mediated recombination process is excluded. Based on the above analysis, the Sn doping into Fe_2O_3 mainly increases the carrier density, further compressing the W_{SCL} resulting in the enhancement of the E_{bi}. Therefore, because the two photoanodes display an identical flat band potential (V_{fb}-0.34 V_{RHE}), they exhibit the same built-in potential under a given applied potential, as well as the same valence band edge energy level (Fig. 1d). This allows to rule out the influence of V_{bi} on the charge transfer kinetics at the

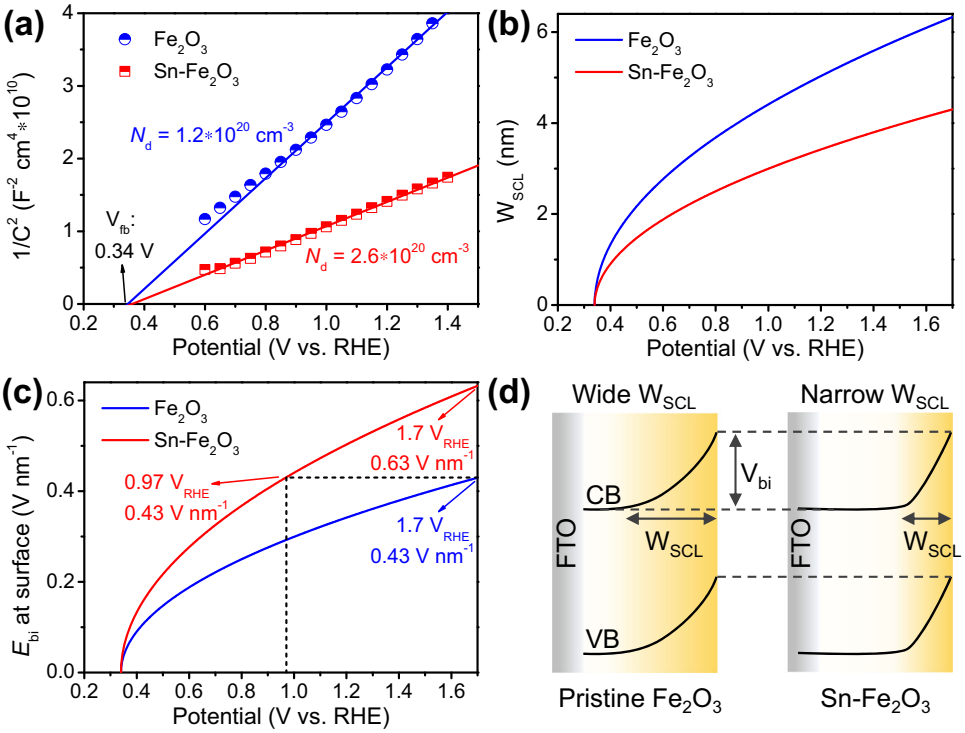

Fig. 1 | The functions of Sn doping into Fe_2O_3. a Mott-Schottky plots (capacitance-potential relationship) of pristine Fe_2O_3 and Sn-Fe_2O_3 photoanodes. Potential-dependent **b** space charge layer width (W_{SCL}), and **c** built-in electric field (E_{bi}) at surface for pristine Fe_2O_3 and Sn-Fe_2O_3 photoanodes. **d** Band bending profiles of pristine Fe_2O_3 and Sn-Fe_2O_3 photoanodes under same applied potential. Test condition: NaOH solution. The potential is not iR corrected.

https://doi.org/10.1038/s41467-026-77786-5

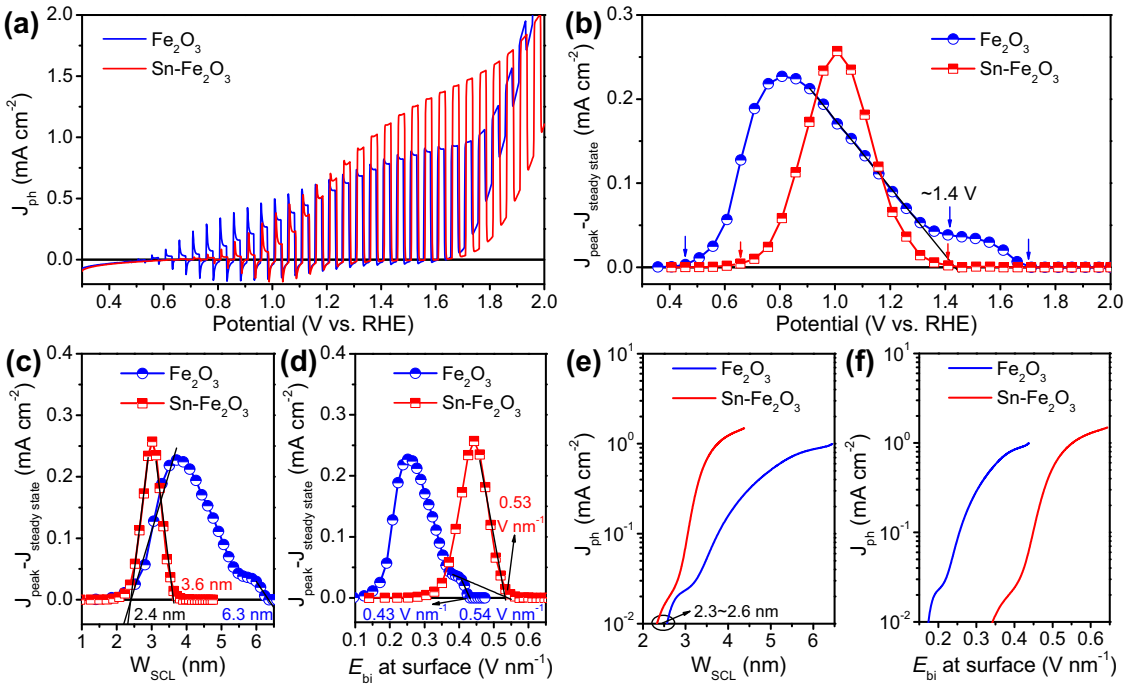

Fig. 2 | PEC performances. a Chopped light LSV and **b** potential-dependent recombination currents (J_{peak}-$J_{steady\ state}$) of pristine Fe_2O_3 and Sn-Fe_2O_3 photoanodes. The recombination current is the difference of photocurrent transient peak at the turning light on and steady-state photocurrent. **c** Correlating recombination currents and W_{SCL}. **d** Correlating recombination currents and E_{bi} at the surface. **e** Correlating steady-state photocurrent and W_{SCL}. **f** Correlating steady-state photocurrent and E_{bi} at surface. The solid black lines are the linear fitting. Test condition: illumination (365 nm LED: 17 mW cm^{-2}); electrolyte: NaOH solution. The potential is not iR corrected. For pristine Fe_2O_3 (1.35 cm^2) and Sn-Fe_2O_3 (1.40 cm^2) photoanodes, the resistances of solution are 48.4 ± 0.1 Ω and 36.3 ± 0.5 Ω, respectively.

semiconductor-solution interface, enabling to disentangle the effect of W_{SCL} and E_{bi} on charge separation.

Impact of band bending profiles on PEC water splitting

The OER activity of pristine Fe_2O_3 and Sn-Fe_2O_3 photoanodes were performed by chopped and continuous light linear sweep voltammetry (LSV). By comparing the photocurrent density (J_{ph}) of pristine Fe_2O_3 and Sn-Fe_2O_3 photoanodes (Fig. 2a and S1b), the Sn-Fe_2O_3 photoanode shows comparable photocurrent with that in pristine Fe_2O_3 at ~ 1.2 V_{RHE}, corresponding to lower photocurrent at onset potential range (<1.2 V_{RHE}), but enhanced photocurrent at high potential range (> 1.2 V_{RHE}). The different PEC performances between two photoanodes may originate from distinct charge dynamics or divergent OER mechanisms. To exclude the effect of Sn doping on the OER mechanisms on the Fe_2O_3 surface, the turnover frequencies (TOF, s^{-1}) and reaction order were measured and calculated by PEC multi-potential steps (PEC-MPS) methodology (Figs. S2, S3, and S11). The nearly identical TOF values at high potential (Fig. S11a), combined with the consistent reaction order transition (Fig. S11b), indicate that the differences in band bending profiles do not govern the interfacial catalytic mechanism. Thus, the different PEC performances at various potential range may be due to the distinct charge dynamics in these two photoanodes.

Next, to understand the different charge separation ability in actual PEC processes, we analyzed the transient spikes under chopped light. Based on the occurred timescale, the transient spikes result from the back recombination process (ms-s) of separated electrons and surface OER intermediates (consumption lifetime > 0.6 s). Consequently, the appearance of transient spikes in onset potential range can reflect the charge separation ability. Figure 2b shows that the onset potentials of transient spike are ~0.45 V_{RHE} and ~0.65 V_{RHE} on pristine Fe_2O_3 and Sn-Fe_2O_3 photoanodes, respectively, suggesting that pristine Fe_2O_3 possesses a higher charge separation ability than Sn-Fe_2O_3 under low applied potentials. To further identify the primary contributor to transient spike in band bending profile of Fe_2O_3, the potential-dependent transient spikes are analyzed with their relationship with the corresponding W_{SCL} and E_{bi}. Crucially, as shown in Fig. 2c, the onset of transient spikes occurs at the same W_{SCL} (2.4 nm) for both photoanodes, even with different E_{bi} values (Fig. 2d). Similarly, Fig. 2e also exhibits that the onset of the steady-state photocurrents occurs at the similar W_{SCL} of 2.3 ~ 2.6 nm on both photoanodes, despite their different E_{bi} values (Fig. 2f). These results indicated that the W_{SCL} of Fe_2O_3 should be at least ~2.4 nm (W_{SCL} threshold) to enable efficient photogenerated charge separation. Given that the [001] direction in the conventional unit cell of α-Fe_2O_3 (c = 13.75 Å) consist of six FeO_6 octahedra units (a FeO_6 octahedra unit is ~2.28 Å)[25], the ~2.4 nm W_{SCL} is about 11 FeO_6 octahedra units. To further confirm the validity of the W_{SCL} threshold, the effect of the condition parameters was investigated, including pH value, illumination intensity, temperature, and electrolyte (Figs. S12–S14). Analogous W_{SCL} of 2.4 ~ 3.0 nm was observed for Fe_2O_3-based photoanodes under the above-mentioned parameters, corroborating the objective validity of the W_{SCL} threshold for reactive charge separation. Additionally, in Figs. S15–S17, other photoanode/electrolyte systems (WO_3, $BiVO_4$ and TiO_2) were also studied in different electrolytes with various pH values (neutral and alkaline). The other photoanodes display W_{SCL} thresholds (WO_3: 0.5 ~ 1.5 nm; $BiVO_4$: 3.0 ~ 7.4 nm; TiO_2: 0.9 ~ 1.1 nm), demonstrating the universal existence of the W_{SCL} threshold in various photoanodes. The different W_{SCL} thresholds imply that the W_{SCL} thresholds in OER are related to the intrinsic properties of photoelectrodes. Furthermore, the W_{SCL} threshold is compared with Debye screening length (λ_D), Thomas-Fermi screening length (l_{TF}), and hole diffusion length (L_D) in Methods and Table S2. Combined with the temperature-dependent W_{SCL} thresholds in Fig. S14, the W_{SCL} thresholds are consistent with the Debye screening lengths, suggesting that the charge screening determines the onset of reactive charge separation.

https://doi.org/10.1038/s41467-026-77786-5

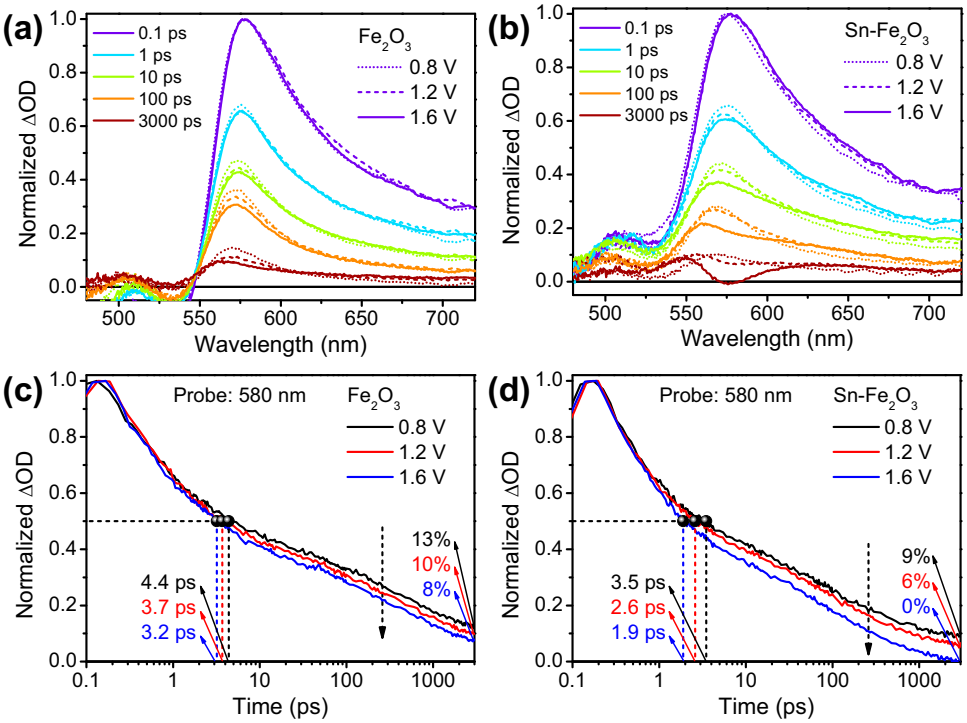

Fig. 3 | Ultrafast charge separation and trapping dynamics. Normalized in-situ fs-TA spectra for **a** pristine Fe_2O_3 and **b** Sn-Fe_2O_3 photoanodes at 0.8, 1.2 and 1.6 V_{RHE} (Fig. S18 shows the raw in-situ fs-TA spectra). Normalized in-situ fs-TA dynamics for **c** pristine Fe_2O_3 and **d** Sn-Fe_2O_3 photoanodes at 0.8, 1.2 and 1.6 V_{RHE}. The normalization in in-situ fs-TA measurements facilitate comparison. The black circles in Fig. 3c and d are the positions of half of the TA amplitude, corresponding to the half-lifetime (a semi-quantitative parameter is used to describe the non-exponential consumption processes). ΔOD is the variation in optical density. Test condition: pump: 400 nm, 100 nJ $pulse^{-1}$ (4×10^{13} photons cm^{-2} $pulse^{-1}$); probe: 450–750 nm; electrolyte: NaOH solution for OER. The potential is not iR corrected.

Then, the disappearance of the transient spikes is used to evaluate the inhibition of back electron recombination by applied high potentials in actual PEC processes. As shown in Fig. 2b, once the applied potential exceeds the potential of the spike peaks, the transient spikes gradually decrease and eventually disappear for both photoanodes as the potential increases further. The disappearance of the spike occurs at a much lower potential for Sn-Fe_2O_3 (~1.4 V_{RHE}) than for pristine Fe_2O_3 (~1.7 V_{RHE}). Correspondingly, the calculated E_{bi} for the disappearance of spikes are 0.43 V nm^{-1} for Fe_2O_3 and 0.53 V nm^{-1} for Sn-Fe_2O_3, while the W_{SCL} are 6.3 nm and 3.6 nm, respectively (Fig. 2d). Nevertheless, different from Sn-Fe_2O_3, the transient spikes on pristine Fe_2O_3 shows three declining stages of 0.8-1.3, 1.3-1.5 and 1.5-1.7 V_{RHE}. When the declining stages of 0.8-1.3 V_{RHE} is subjected to linear fitting, there is an intercept of ~1.4 V_{RHE}, which is closed to the disappeared potential of transient spike on Sn-Fe_2O_3. This ~1.4 V_{RHE} potential is also comparable to the reported potential of completely blocking the back electron flow (~1.3 V_{RHE}) on FTO/SiO_2/Si-doped Fe_2O_3 photoanode[26], suggesting that the blocking of back electron recombination is a thermodynamics-dominated process (V_{bi}: ~1.06 eV). Above 1.4 V_{RHE}, the transient spikes on pristine Fe_2O_3 should be caused by other factor, which can be modulated by the E_{bi} in space charge layer. To exclude the possible interference of electrocatalytic OER for PEC transient spikes, the transient spikes at 1.4-1.6 V_{RHE} for pristine Fe_2O_3 and 1.1-1.3 V_{RHE} for Sn-Fe_2O_3 are linear fitting. When the transient spikes are disappeared, two photoanodes displays a similar E_{bi} (Fe_2O_3: ~0.54 V nm^{-1}, Sn-Fe_2O_3: ~0.53 V nm^{-1}). Thus, the E_{bi} plays dominant roles in inhibiting back recombination through transient spikes, once the W_{SCL} is larger than the threshold for charge separation.

Band bending profile modulated charge dynamics in the water oxidation reaction

To understand the effect of band bending profiles on ultrafast charge separation and transfer, the in-situ fs-transient absorption (fs-TA) spectra and dynamics were investigated under three typical potentials of 0.8, 1.2 and 1.6 V_{RHE} (Fig. 3). These three potentials were selected based on the photocurrents of the two photoanodes (Fig. 2a and S1b), which display three potential intervals of <1.2 V_{RHE} ($J_{Fe2O3} > J_{Sn\text{-}Fe2O3}$), ~1.2 V_{RHE} ($J_{Fe2O3} \approx J_{Sn\text{-}Fe2O3}$), and >1.2 V_{RHE} ($J_{Fe2O3} < J_{Sn\text{-}Fe2O3}$). Figure 3a and b show the normalized in-situ fs-TA spectra of pristine Fe_2O_3 and Sn-Fe_2O_3 photoanodes, in which two photoanodes display a similar positive absorption band with a peak at ~580 nm probe wavelength, in accord with previous reports[13,27]. The difference of spectral traces at wavelengths shorter than 550 nm might be originated from the partial substitution of Fe atoms by Sn atoms, resulting in decrease of d-d transition (Fe→Fe) and ligand-to-metal charge transfer (O→Fe)[28–30]. Under all potentials (0.8, 1.2 and 1.6 V_{RHE}), the fs-TA spectra at 0.1 ps are overlapped for each specific photoanode, suggesting a potential-independent charge generation dynamics. When the time delays are longer than 1ps, the TA amplitudes decrease with increasing applied potentials. More importantly, Sn-Fe_2O_3 exhibits more profound decrease than Fe_2O_3, resulting in a different spectral shape with time delay over 100 ps. At 3 ns, the TA peak of ~570 nm at 0.8 V_{RHE} becomes an absorption valley at 1.2 and 1.6 V_{RHE} in Sn-Fe_2O_3, while the TA peak of pristine Fe_2O_3 only exhibits a blue shift from 570 nm (0.8 V_{RHE}) to 568 nm (1.2 V_{RHE}) finally to 560 nm (1.6 V_{RHE}). The absorption valley should be assigned to a bleaching signal of 580 nm, which is originated from the ultrafast electron trapping process in space charge layer[13]. The absorption valley in Sn-Fe_2O_3 demonstrates that more photogenerated electrons are captured by electron trap states than that in Fe_2O_3.

https://doi.org/10.1038/s41467-026-77786-5

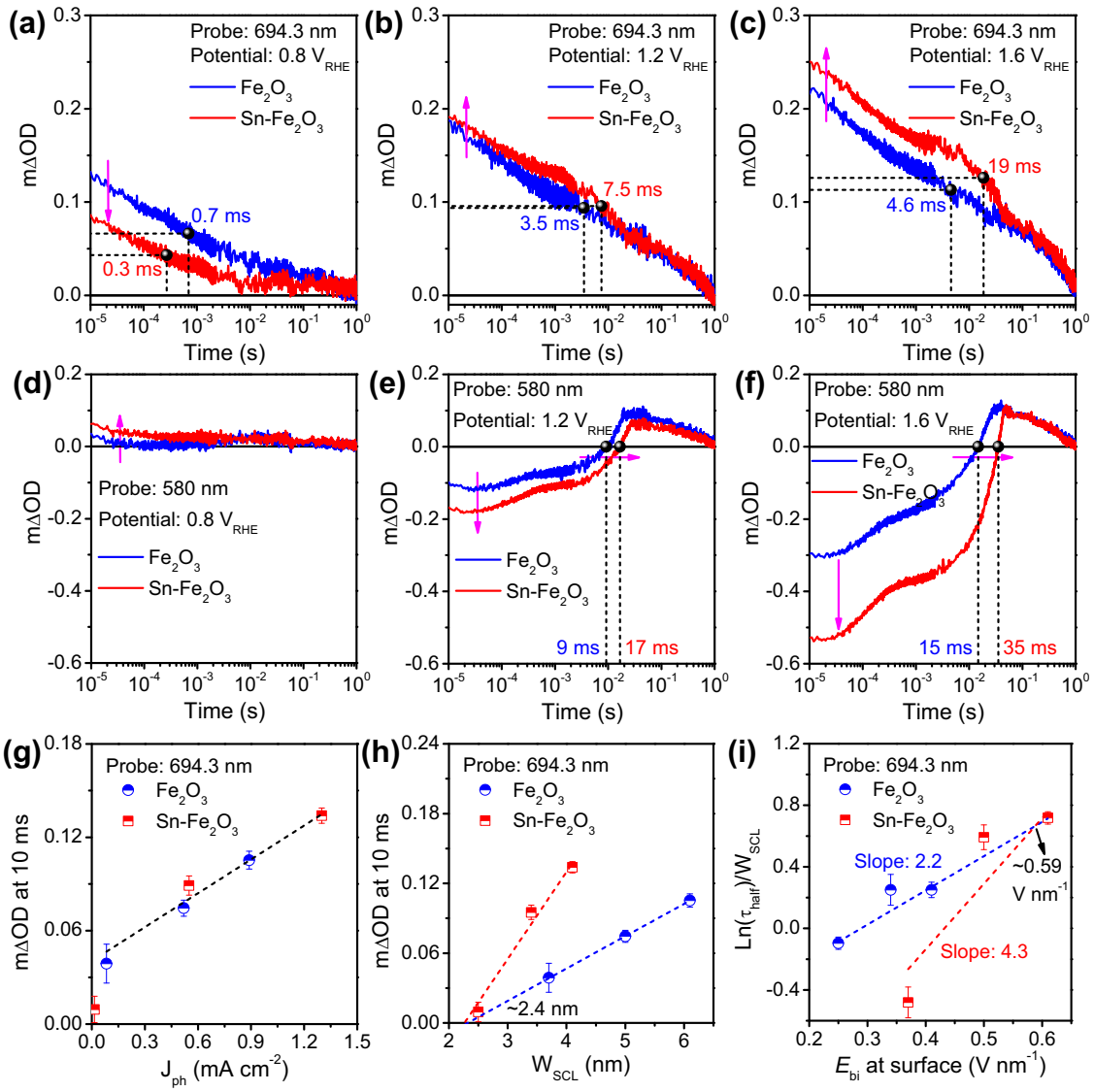

Fig. 4 | Hole transfer and electron de-trapping processes. Comparing the in-situ μs-s TA dynamics of two photoanodes at 694.3 nm probe (**a**–**c**) (the black circles are the positions of half of the TA amplitude, corresponding to the half-lifetime), and 580 nm probe (**d**–**f**) (the black circles are the positions of the zero TA amplitude). **g** Correlating TA amplitudes of 694.3 nm at 10 ms and steady-state photocurrents. **h** Correlating TA amplitudes at 10 ms and W_{SCL}. **i** Correlating half-lifetime and E_{bi}. The dashed lines are the linear fitting. Error bars in Figs. 4g–i represent the standard deviation of measurement noise. ΔOD is the variation in optical density, and mΔOD = ΔOD × 1000. Test condition: pump: 355 nm, 300 μJ pulse^{-1} (6.8×10^{14} photons cm^{-2} pulse^{-1}); electrolyte: NaOH solution for OER. The potential is not iR corrected.

To further quantify the ultrafast charge trapping and separation ability at different band bending profiles, the in-situ fs-TA dynamics of two photoanodes were compared. The fs-TA profiles in Fig. 3c and d display potential-independent (<1 ps) and potential-dependent (1-3000 ps) decay dynamics, which should be assigned to the relaxation processes via metal-centered ligand field states and polaron states, respectively[27]. With the potential increase, pristine Fe_2O_3 photoanode shows accelerated half-lifetimes from 4.4 ps (0.8 V_{RHE}) to 3.2 ps (1.6 V_{RHE}) resulting in reduced TA amplitude at 3 ns from 13% (0.8 V_{RHE}) to 8% (1.6 V_{RHE}) of the initial amplitude. Similarly, Sn-Fe_2O_3 photoanode also displays accelerated lifetimes and reduced TA amplitude at 3 ns. The accelerated lifetimes and reduced TA amplitude are assigned to the promoted electron trapping processes, which reflect the enhanced charge separation with applied potentials increasing[13,17]. By comparing the fs-TA dynamics of Fe_2O_3 and Sn-Fe_2O_3, the shorter lifetimes and lower TA amplitude at 3 ns indicate the more efficient charge separation in Sn-Fe_2O_3.

Furthermore, to confirm the promoted charge separation by high potentials, the photoinduced hole signal was studied at 650 nm probe wavelength (Fig. S19). With increasing the potentials, both Fe_2O_3 and Sn-Fe_2O_3 photoanodes display prolonged lifetimes and increased holes at 3 ns, demonstrating the improved charge separation by applied potentials. Under the same applied potential, the more significant charge separation in Sn-Fe_2O_3 photoanode relative to that of pristine Fe_2O_3 implies that the strong E_{bi} has an essential role in promoting ultrafast charge separation, which is also demonstrated by the global fitting results for in-situ fs-TA spectra of two photoanodes (Fig. S20). Nevertheless, the promotion of ultrafast charge separation in the Sn-Fe2O3 photoanode across all potentials is inconsistent with their PEC performance, indicating that ultrafast charge separation is not the determining factor in the actual PEC process. Thus, the charge dynamics on the μs-s timescale for OER may be the crucial factor, contributing to the actual PEC process directly.

To further reveal the governing function of band bending profile on PEC water splitting, in-situ TA dynamics of pristine Fe_2O_3 and Sn-

Fe_2O_3 photoanodes at μs-s timescale were studied at two typical probe wavelengths (Fig. 4), in which the 580 nm and 694.3 nm probes are the signals of trapped electron and photoinduced hole, respectively[15,31]. According to the photocurrent curves of two photoanodes in Fig. 2a, the TA dynamics at 0.8, 1.2 and 1.6 V_{RHE} are investigated (PEC parameters are listed in Table S1). In Fig. 4a–c, two photoanodes exhibit increased TA amplitudes and extended lifetimes at 694.3 nm with increasing applied potentials, reflecting the increase of long-lived holes for PEC water oxidation. When comparing the TA dynamics, the two photoanodes exhibit obvious differences at different potentials. Under 0.8 V_{RHE} (Fig. 4a), the pristine Fe_2O_3 shows larger TA amplitude (0.13 mΔOD at 10 μs) and longer lifetime (0.7 ms) than that in Sn-Fe_2O_3 (0.07 mΔOD and 0.3 ms), in accord with the higher photocurrent in pristine Fe_2O_3 photoanode. Considering the W_{SCL} and E_{bi} in pristine Fe_2O_3 (W_{SCL}: 3.7 nm, E_{bi}: 0.25 V nm^{-1}) and Sn-Fe_2O_3 (W_{SCL}: 2.5 nm, E_{bi}: 0.37 V nm^{-1}) at 0.8 V_{RHE}, it illustrates that the W_{SCL} plays a dominant role under low applied potentials, enabling effective charge separation for surface reactions despite the severe back recombination due to the limited E_{bi}. As the potential increases to 1.2 V_{RHE} (Fig. 4b), Fe_2O_3 and Sn-Fe_2O_3 photoanodes show comparable TA amplitude (~0.19 mΔOD at 10 μs), but Sn-Fe_2O_3 displays longer lifetime (7.5 ms) than the pristine Sn-Fe_2O_3 (3.5 ms). The comparable TA amplitude demonstrates that the larger W_{SCL} of 5.0 nm and smaller E_{bi} of 0.34 V nm^{-1} in pristine Fe_2O_3 result in similar amounts of long-lived holes as the smaller W_{SCL} of 3.4 nm and larger E_{bi} of 0.50 V nm^{-1} in Sn-Fe_2O_3, which may be the kinetic reasons for the comparable photocurrent on the two photoanodes at 1.2 V_{RHE}. These results indicate that the trade-off is achieved between the charge separation (W_{SCL}) across the space charge layer and the charge loss (E_{bi}) due to back recombination. With the potential further increase to 1.6 V_{RHE} (Fig. 4c), Sn-Fe_2O_3 shows a larger TA amplitude (0.25 mΔOD at 10 μs) and longer lifetime (19 ms) than that in pristine Fe_2O_3 (0.22 mΔOD and 4.6 ms). This implies that the more long-lived holes in Sn-Fe_2O_3 photoanode will contribute to surface OER, in accord with the improved photocurrent at 1.6 V_{RHE}. In addition, the nearly overlapping TA curves at 0.04-1 s indicate same water oxidation rate on two photoanodes in Fig. S21, in line with the TOFs and rate law analysis in Figure S11. The increased long-lived holes in Sn-Fe_2O_3 demonstrates the dominant role of E_{bi} under high potentials, since the E_{bi} of Sn-Fe_2O_3 is larger than Fe_2O_3 while W_{SCL} is narrower in Sn-Fe_2O_3.

To further confirm the charge dynamics in actual PEC processes, the potential-dependent μs-s TA results were studied at 580 nm wavelength to investigate the trapped electrons (Fig. 4d–f), because the 580 nm bleach signal is assigned to the capture for photogenerated electrons in the emptied electron trap states which are induced by the E_{bi} in space charge layer. Namely, the intensity of bleach signal simultaneously reflects both the number of E_{bi}-emptied electron trap states and the number of photogenerated electrons captured by these trap states. Pristine Fe_2O_3 shows lower absorption amplitude than Sn-Fe_2O_3 at 0.8 V_{RHE} (Fig. 4d), indicating more trapped electrons. At high potentials of 1.2 and 1.6 V_{RHE} (Fig. 4e and f), both photoanodes show bleach signal, which increase with applied potential increasing. The bleach signal in Sn-Fe_2O_3 is much larger than that in Fe_2O_3. More importantly, for both photoanodes, increasing applied potentials delays the zero-crossing point of the TA signal. This delay indicates that the back recombination is suppressed by the reverse built-in electric field (E_{bi}). At the same high potential, the Sn-Fe_2O_3 photoanode displays a longer time of zero-crossing point (1.2 V_{RHE}: 17 ms; 1.6 V_{RHE}: 35 ms) than that in the pristine Fe_2O_3 photoanode (1.2 V_{RHE}: 9.2 ms; 1.6 V_{RHE}: 15 ms), indicating the longer charge lifetimes in Sn-Fe_2O_3 photoanode. These results indicate the increased long-lived electrons in Sn-Fe_2O_3 at high potentials, which is consistent with the increased long-lived holes discussed above. The μs-s TA dynamics closely match the PEC performances at various applied potentials, indicating that charge dynamics at μs-s timescales directly govern the PEC reactions. The charge separation is primarily improved by the W_{SCL} under low applied potentials, which may result from the spatial separation across the space charge layer. Under high applied potentials, the suppression of back recombination by the E_{bi} (reverse built-in electric field) becomes dominant, ensuring long-lived charges for PEC reactions.

To quantify the correlation between the band-bending profile and charge dynamics, the TA amplitudes and half-lifetimes are linked to the W_{SCL} and E_{bi}. For two photoanodes, there is a good linear relationship between TA amplitudes of 694.3 nm at 10 ms (long-lived holes) and steady-state photocurrents (Fig. 4g), indicating the hole density-dominated OER kinetics. When linking the TA amplitudes of 694.3 nm at 10 ms and the W_{SCL} (the relationship of $[h^+] \propto W_{SCL}$ is derived in Note S1), the onsets of long-lived hole signal on both photoanodes occur at the same W_{SCL} (~2.4 nm) (Fig. 4h), consistent with the observed W_{SCL} threshold in Fig. 2c and d. Then, Fig. 4i shows that the half-lifetimes of hole on two photoanodes are prolonged by the increasing E_{bi}, suggesting the E_{bi}-dominated charge recombination processes. By linear fitting (the relationship of $Ln(\tau_{half})/W_{SCL} \propto E_{bi}$ is derived in Note S1, and the relationship of $Ln(\tau_{half}) \propto E_{bi}$ is shown in Figure S21d), pristine Fe_2O_3 photoanode displays a smaller E_{bi} onset and slope than Sn-Fe_2O_3 photoanode, resulting in a point of intersection (~0.59 V nm^{-1}). The E_{bi} at the point of intersection is ~0.57 V nm^{-1}, close to the E_{bi} of spike disappearance for pristine Fe_2O_3 (0.54 V nm^{-1}) and Sn-Fe_2O_3 (0.53 V nm^{-1}) photoanodes in Fig. 2c, demonstrating that the E_{bi} plays the key role in suppressing back electron recombination.

Impact of W_{SCL} and E_{bi} in PEC processes

The Fe_2O_3 and Sn-Fe_2O_3 photoanodes with identical flat band potential were employed to disentangle the impact of W_{SCL} and E_{bi} on charge dynamics in PEC reactions. With higher density of majority carrier, the band bending profile in Sn-Fe_2O_3 exhibit narrower W_{SCL} and larger E_{bi} than that in Fe_2O_3 under the same applied potentials, resulting in sharp and mild band bending profiles in Sn-Fe_2O_3 and Fe_2O_3 respectively. In combination with PEC performances, both fs-ns and μs-s TA spectroscopy were used to understand the governing role of band bending profile in PEC water oxidation. In in-situ fs-s TA results, Sn-Fe_2O_3 exhibits accelerated electron trapping and improved charge separation than pristine Fe_2O_3, even for narrow W_{SCL} of 2.5 nm at 0.8 V_{RHE}. This indicates that the sharp band bending profiles with stronger E_{bi} facilitate initial charge separation at the fs-ns timescale under various applied potentials. Although this ultrafast charge separation is enhanced in Sn-Fe_2O_3, its PEC performance at low potentials remains poor, demonstrating the processes on this timescale are not the determining factor for PEC reaction. More importantly, the in-situ μs-s TA results are in good accordance with PEC performances, revealing the underlying mechanisms of width of space charge layer (W_{SCL}) and built-in electric field (E_{bi}) on reactive charge dynamics. Figure S22 displays the kinetic framework linking ultrafast charge generation to steady-state OER, where the recombination process has always existed. Because the ultrafast charge separation is the precondition of subsequent catalytic reaction, the ultrafast enhancements in Sn-Fe_2O_3 indirectly contribute to PEC performances. The governing role of band bending profiles on charge dynamics in PEC reaction are summarized schematically in Fig. 5.

When the applied potential is changed from the flat band potential (V_{fb}: 0.34 V_{RHE}) to a low potential of <1.2 V_{RHE} (for example, 0.8 V_{RHE}), the energy band of pristine Fe_2O_3 and Sn-Fe_2O_3 undergoes a transition from flat band to bending band (Fig. 5a–b, or Fig. 5a–c). For the pristine Fe_2O_3 photoanode (Fig. 5b), the wider W_{SCL} (3.7 nm at 0.8 V_{RHE}) facilitates the migration of more photoinduced charges over a larger distance, resulting in spatial charge separation of more photoinduced charges. On the other hand, in Sn-Fe_2O_3, the narrower W_{SCL} (2.5 nm) only drives fewer photoinduced charge migration across a smaller distance (Fig. 5c). Although the larger E_{bi} (0.37 V nm^{-1} at 0.8

https://doi.org/10.1038/s41467-026-77786-5

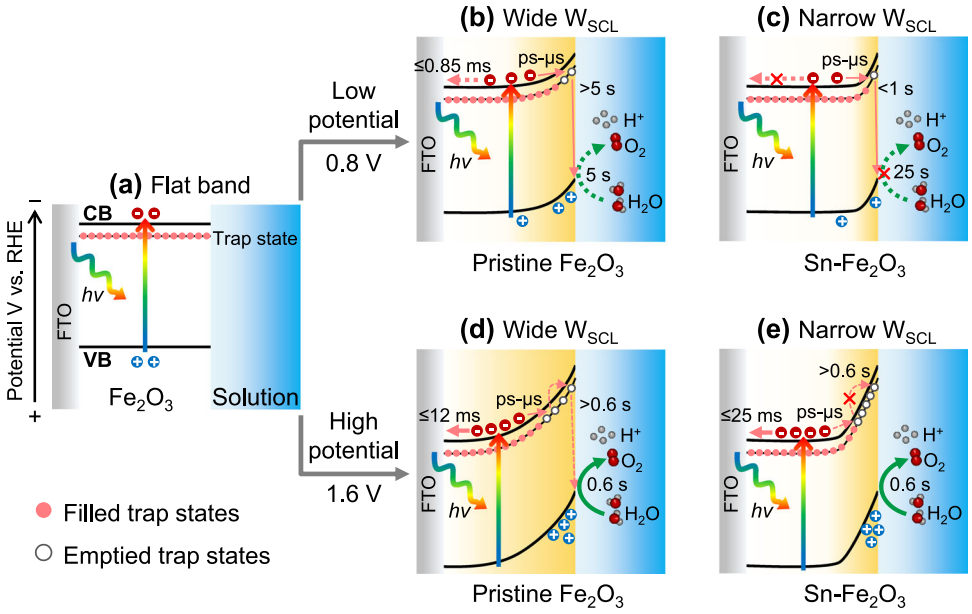

Fig. 5 | The effect of band bending profiles on charge trapping, transfer, and recombination. a flat band; **b** wide W_{SCL} in pristine Fe_2O_3 and **c** narrow W_{SCL} in Sn-Fe_2O_3 at low potential; **d** wide W_{SCL} in pristine Fe_2O_3 and **e** narrow W_{SCL} in Sn-Fe_2O_3 at high potential. The charge flow direction is denoted by arrow '→', and the solid and dashed arrows represent the relative quantity of each process; the '×' indicates no transfer. The electron trap time is extracted from in-situ fs-s TA dynamics (the formation times of 580 nm bleach reflect the electron trap process); the extraction time of trapped electrons is obtained from the time of bleach recovery at 580 nm in μs-s TA dynamics (Table S3, Figs. S21b and S21c); the OER lifetime is extracted from the calculated TOF values (Fig. S11a); the lifetime via trap-mediated recombination is obtained from the TOF values (Fig. S11a) or μs-s TA dynamics (Fig. 4a).

V_{RHE}) may suppress back recombination more efficiently in Sn-Fe_2O_3, fewer long-lived charges exist in Sn-Fe_2O_3 for PEC reactions. Consequently, at low potential, pristine Fe_2O_3 photoanode possesses more long-lived holes to produce higher photocurrent. These results indicate that W_{SCL} dominates PEC charge dynamics at low potentials through spatial charge separation. Thus, a threshold of W_{SCL} for PEC charge separation is observed to be 2.4 nm. Given that the low potential of 0.8 V_{RHE} is close to the open-circuit potential (OCP) of Fe_2O_3 photoanodes, constructing Fe_2O_3 photoanodes with a wide W_{SCL} (significantly larger than the 2.4 nm threshold) is crucial for lowering the OCP and enabling unbiased PEC reactions.

When the potential is further increased to a high potential of >1.2 V_{RHE} (for example,1.6 V_{RHE}), the W_{SCL} in both photoanodes is increased to much larger than the 2.4 nm threshold, with E_{bi} increased as well (Fig. 5d, e). The E_{bi} is not only capable of separating photoinduced charges, but also emptying the trapped intrinsic electrons. Compared with the E_{bi} on pristine Fe_2O_3 photoanode (0.41 V nm^{-1}), the stronger E_{bi} on Sn-Fe_2O_3 photoanode (0.61 V nm^{-1}) effectively empties the trapped intrinsic electrons in space charge layer (Fig. 5e). These unfilled trap states will capture photogenerated electrons, resulting in larger changes of spectral shape and bleach intensity for Sn-Fe_2O_3 (the in-situ fs-s TA results in Figs. 3 and 4). Moreover, the stronger E_{bi} in Sn-Fe_2O_3 photoanode ensures slower back electron recombination, thereby resulting in more long-lived holes. Thus, under high potential, Sn-Fe_2O_3 photoanode exhibits higher OER photocurrent. Nevertheless, from a thermodynamic perspective, both pristine Fe_2O_3 and Sn-Fe_2O_3 should be capable of blocking the recombination processes of back electrons and charged OER intermediates, due to the same V_{bi}. However, transient spikes are still observed on the pristine Fe_2O_3 photoanode at high potentials (Fig. 2). Through comparing the difference of two photoanodes at high potential, the transient spikes on pristine Fe_2O_3 should be originated from the insufficient emptying of intrinsic electrons in the space charge layer due to the lower driving force of the E_{bi}. These trapped intrinsic electrons will hinder the further capture for photogenerated electrons, resulting in the minor changes of trapped electron signal (dynamics of 580 nm probe in the in-situ fs-s TA results), in line with previous reports[13,14,18,20,32]. Under chop light, by the cascaded electron transfer (Fig. 5d), these trapped electrons will lead to the back current. Namely, under high potential, the strong E_{bi} in the n-type doping into Fe_2O_3 (Sn in our case) effectively empties the trapped intrinsic electrons and blocks the back electron transfer processes, more beneficial to surface catalytic processes than the pristine Fe_2O_3 photoanode.

Based on the above analysis of charge dynamics in Fe_2O_3-based photoanodes, this study provides insights about the role of band bending profile (W_{SCL} and E_{bi}) in PEC water splitting. Through disentangling the contribution of W_{SCL} and E_{bi} to charge dynamics in water oxidation reaction, W_{SCL} determines the onset of OER photocurrent, resulting in a W_{SCL} threshold (2.4 nm) for reactive charges; and E_{bi} plays a key role in blocking back electron recombination. Sn element doping significantly increases the density of majority carrier in Fe_2O_3 to simultaneously narrow the W_{SCL} and increase the E_{bi} in band bending profile, resulting in a positive shift of photocurrent onset (the case at low potential), and improved photocurrent under high potential. Although the PEC performances on pristine Fe_2O_3 and Sn-Fe_2O_3 photoanodes are consistent with previous reports about undoped/doped Fe_2O_3 photoanodes (Ti, Sn, Si, Ta, Sb, etc.)[13,31,33–35], our mechanism analysis indicates that the functions of element doping are assigned to the band bending profile, but not due to the change of carrier mobility, transportation resistance and surface states. According to the above finding, we propose that combining the advantages of different band bending profiles is a promising pathway to accelerate ultrafast charge separation (fs-ns timescale), and block recombination between back electrons and charged OER intermediates (μs-s), for example, constructing multiple Fe_2O_3 layer with different doping concentration (FTO|Sn-Fe_2O_3|Fe_2O_3 or gradient doping). Furthermore, optimizing the charge screening of photoelectrode for reactant (water oxidation: OH^-[36]) to modulate activation free energy[37] will contribute to reducing the photocurrent onset potential. For WO_3, $BiVO_4$ and TiO_2 photoanodes, the narrow W_{SCL} thresholds imply the facile efficient charge separation, indicating that the key lies in optimizing the E_{bi}.

In this work, we take pristine Fe_2O_3 and Sn-doped Fe_2O_3 photoanodes as a model system to comprehensively study the mechanisms of band bending profiles in photogenerated charge dynamics, and disentangle the contribution of W_{SCL} and E_{bi} to PEC water oxidation reaction. We have found that the W_{SCL} in band bending profile exhibits a threshold of ~2.4 nm for reactive charge separation, which determining the photocurrent onset, and the back electron recombination is mainly prohibited by the E_{bi}. Above the photocurrent onset potential, the *E*bi in band bending profile will promote the depletion of intrinsic electrons in electron trap states, thereby trapping photoinduced electrons to facilitate spatial separation of photoinduced electron-hole pairs. More importantly, the strong E_{bi} in band bending profile is sufficient to block the recombination process of back electrons and charged OER intermediates. It shows that engineering the band bending profile and charge screening at the photo(electro)catalyst-solution interface is a promising approach to enhance the photo(electro)catalytic efficiency.

Methods

Materials

Chemicals during synthesis and measurement were used without further purification.

Preparation of FeOOH films

FeOOH films were prepared by the solvothermal deposition method[16]. The conductive substrates of FTO (1 cm × 3.5 cm, 14 Ω sq^{-1}, Wuhan Lattice Solar Energy Technology Co., Ltd.) were first cleaned in acetone (Sinopharm, 99.5%), isopropanol (Sinopharm, >99.7%), ethanol (Sinopharm, >99.7%), and deionized water for 20 minutes, respectively. The non-conductive side of clean FTO was masked with tape and placed against the wall of the bottle (20 mL). Then, 14 mL solution containing 0.15 M $FeCl_3$ (Innochem, 98%) and 1 M $LiNO_3$ (Innochem, 99%) was added. The bottle was sealed and placed in the oven at 100 °C for 1 h. Finally, the deposited FeOOH films were washed with deionized water.

Surface doping with tin (Sn)

For the surface doping of Sn[16], the FeOOH film was immersed in the $SnCl_2$ ethanol solution (0.1 M, 15 mL, Innochem, 99%) for 10 min. The film was blown off with compressed air. Then, the FeOOH films with/without Sn doping were annealed at 550 °C for 3 h, followed by a heat treatment at 800 °C for 15 min. The obtained sample without Sn was labeled as Fe_2O_3. The obtained sample with Sn doping was labeled as Sn-Fe_2O_3.

Preparation of WO_3 and Sn-WO_3 films

WO_3 films were prepared via a sequential procedure of chemical bath deposition and high-temperature calcination[38]. In detail, $Na_2WO_4{\cdot}2H_2O$ (0.4 g, Innochem, 98%) and $(NH_4)_2C_2O_4$ (0.15 g, Innochem, 99%) were dissolved in deionized water (33 mL). After dissolution, the HCl (9 mL, Sinopharm, 37 %), H_2O_2 (8 mL, Sinopharm, 30 %) and ethanol (30 mL) were added sequentially with vigorous magnetic stirring for 20 min. The cleaned FTO glasses (1 cm × 4 cm) were immersed in above solution, followed chemical bath deposition at 90 °C. After 2 h, the films were taken out, washed with deionized water, and dried in oven (60 °C, 2 h). The surface Sn doping was conducted through immersing above film into $SnCl_2$-ethanol solution (0.1 M, 15 mL) for 10 min. After taking out the films, the residue solution was blown off by compressed air. After further annealing in air at 600 °C for 2 h, the WO_3 and Sn-WO_3 films were obtained.

Preparation of $BiVO_4$ and W-$BiVO_4$ films

$BiVO_4$ films were prepared through a metal-organic decomposition method[38]. Briefly, $Bi(NO_3)_3{\cdot}5H_2O$-acetic acid solution (1.5 mL, 0.4 $mol{\cdot}L^{-1}$; $Bi(NO_3)_3{\cdot}5H_2O$: Alfa Aesar, 98%; acetic acid: Sinopharm, 99.5%), and vanadiumoxy acetylacetonate-acetylacetone solution (20 mL, 0.03 $mol{\cdot}L^{-1}$; vanadiumoxy acetylacetonate: ACROS, 99%; acetylacetone: Sinopharm, 99%) were prepared and stirred at 90 °C for 1 h. The mixture of the two solutions was further stirred at 50 °C for 1 h. Through spinning (1000 rpm for 20 s) the mixture on FTO (2 cm × 2 cm), the precursor films were obtained. $BiVO_4$ films were obtained by calcining the precursor films at 450 °C for 10 min. The spin-coating/calcination process was repeated 8 times to increase the film thickness. After spinning the 8th layer, the calcination at 450 °C for 10 h was conducted to ensure the crystallinity. The surface W doping was conducted through immersing $BiVO_4$ film into Na_2WO_4-H_2O solution (0.1 M, 15 mL) for 10 min. After taking out the films, the residue solution was blown off by compressed air. After further annealing in air at 450 °C for 2 h, the $BiVO_4$ and W-$BiVO_4$ films were obtained.

Preparation of TiO_2 and Al-TiO_2 films

TiO_2 films were prepared by a hydrothermal deposition method[38]. In detail, titanium tetraisopropanolate (1 mL, Sinopharm, 99%) was added HCl solution (55 mL, Sinopharm, 16.8%) and stirred for 1 h. The solution and cleaned FTO (2 cm × 4 cm) were put into a Teflon-lined stainless autoclave (100 mL). After hydrothermal deposition (220 °C for 20 min in an oven) and washing, the rutile TiO_2 films were obtained. A further calcination at 400 °C for 1 h was conducted to remove the residual organics. The surface Al doping was conducted through immersing TiO_2 film into $Al_2(SO_4)_3$-H_2O solution (0.1 M, 15 mL, BKMAM, >99%) for 10 min. After taking out the films, the residue solution was blown off by compressed air. After further annealing in air at 450 °C for 2 h, the TiO_2 and Al-TiO_2 films were obtained.

Morphological and structural characterization

The absorption spectra of hematite films were acquired using a home-built UV-VIS-NIR spectrophotometer (Avantase). The surface morphology was characterised by scanning electron microscopy (SEM). The crystal structure was analyzed by X-ray Diffraction (XRD, Rigaku, SmartLab SE). X-ray photoelectron spectroscopy (XPS, ESCALAB 250X Thermo Fisher Scientific, monochromatic Al Kα source) and XPS depth profiling (Ar^+ etching, 3 kV) were carried out to analyze the chemical composition.

(Photo)electrochemical measurements

(Photo)electrochemical measurements were performed in a quartz cell (5 cm × 5 cm × 5 cm, Fig. S23) through a three-electrode system. The working electrode was Fe_2O_3 or Sn-Fe_2O_3 films coated with epoxy, the counter electrode was a Pt plate (1 cm × 2 cm), and the reference electrode was an Ag/AgCl/saturated KCl, which was calibrated against another standard Ag/AgCl/saturated KCl electrode. The electrolyte was NaOH solution (1 M, 30 mL, Innochem, 99%), which was freshly prepared and stored in sealed glass vials before use. All applied potential was converted to the reversible hydrogen electrode (RHE) using the Nernst equation: E_{RHE} (V) = $E_{Ag/AgCl}$ (V) + 0.0591·pH + $E^0_{Ag/AgCl}$, where E_{RHE} is the applied potential versus RHE, $E_{Ag/AgCl}$ is the measured potential versus Ag/AgCl/saturated KCl reference electrode, and $E^0_{Ag/AgCl}$ is the standard potential of the Ag/AgCl/saturated KCl reference electrode versus RHE at 25 °C (0.1981 V versus RHE). Mott-Schottky measurements were carried out by CHI 660 f at a frequency of 1 kHz with a 5 mV amplitude sinusoidal voltage pulse. All (photo) electrochemical experiments were conducted at room temperature (~25 °C) and controlled by the instrument's proprietary software of CHI 660 f potentiostat. In temperature-dependent PEC measurements, the solution temperature was held at the desired value by a hotplate. Through temperature correction, E_{RHE} (V) = − 0.001·(T − 273.15) + $E^0_{Ag/AgCl}$ + $E_{Ag/AgCl}$ (V) + 0.0002·T·pH, where T (K) is the absolute temperature in Kelvin.

Photoelectrochemical-multi-potential steps (PEC-MPS) technique

The PEC-MPS measurements were conducted using a sequence of three successive potential steps[38,39]. During each sequence, the working electrode was initially held at a low potential (E_{low} is 0.6 V_{RHE} for Fe_2O_3 and Sn-Fe_2O_3 photoanodes) for 10 s, then stepped to a higher potential ($E_{high} \geq E_{low}$) for another 10 s, and finally returned to the initial E_{low} for an additional 10 s. The current was sampled at 0.002 s intervals throughout the entire acquisition period. The steady-state current was obtained at the end of the 10 s high-potential segment, while the charge accumulated during the high potential step was derived by integrating the current transient over the second low-potential segment. By changing E_{high}, the potential dependences of photo-/dark-currents and photo-/dark-charges were obtained. The difference of current/charge under illumination and in the dark was the absolute photoinduced current/charge. The PEC-MPS measurements for Fe_2O_3 and Sn-Fe_2O_3 photoanodes were performed only once, thereby yielding a set of TOFs.

Femtosecond transient absorption (fs-TA) spectroscopy

The fs-TA spectra were recorded using a custom-built experimental setup. Briefly, a femtosecond titanium sapphire laser (800 nm, 35 fs, 1 kHz, Spitfire Ace, Spectra Physics) served as the laser source. The excitation beam (laser spot diameter: 800 μm) was generated by an optical parametric amplifier (TOPAS, Spectra Physics). A visible probe light was produced by focusing the 800 nm laser onto a sapphire crystal plate, and a fiber optic spectrometer (AvaSpec-ULS2048CL-EVO, Avantes) was used to detect the visible probe light, which ranged from 400 to 800 nm. The in-situ TA experiments were conducted by a three-electrode setup controlled by a CHI 660 f potentiostat in NaOH solution. During in-situ fs-TA measurements, a constant potential was controlled by chronoamperometry.

μs-s TA spectroscopy

During μs-s TA measurements, the pump pulse was generated by the third harmonic of a Nd: YAG laser (EKSPLA, NT 342B, 355 nm, a pulse width of 5 ns, a repetition rate of 0.9 Hz, and a beam diameter of 1 cm). The pulse was delivered to the sample through a liquid light guide, yielding an incident pump energy of approximately 300 μJ per pulse. Probe light was provided by a 100 W tungsten lamp (Bentham, IL 1) coupled to a monochromator (Zolix, Omni - λ 300). The transmitted probe light was detected by a Si photodiode (Hamamatsu), and the variation of optical density (ΔOD) was recorded concurrently by an oscilloscope (Tektronix, TDS 2012C) and a data acquisition card (National Instruments NI-6221). Each transient curve was averaged over 400 laser shots. The in-situ μs-s TA experiments were carried out via chronoamperometry controlled by a CHI 760E potentiostat.

(P)EIS and DRT analysis

(P)EIS of the photoanode was performed from 105Hz to 100Hz with a signal amplitude of 5mV through an electrochemical workstation (CHI 660f). The bulk resistances of Fe_2O_3 and Sn-Fe_2O_3 photoanodes were obtained by fitting the equivalent circuit and DRT analysis. The equivalent circuit was fitted using Zview software. The DRT analysis was conducted using an open-source MATLAB code[40].

Calculation of the parameters of band bending profile

N_d is calculated by the Mott-Schottky equation[12]:

$$\frac{1}{C^2} = \frac{2}{\varepsilon_0 \varepsilon_r A^2 e N_d}\left(V - V_{fb} - \frac{k_B T}{e}\right)$$

where C (F) is the space-charge-layer capacitance; ε_0 is the vacuum permittivity (8.854×10^{-12} F m^{-1}); ε_r is the relative permittivity of Fe_2O_3 (32); A (cm^2) is the geometric area; e is the electronic charge (1.602×10^{-19} C); V (V_{RHE}) is the applied potential; V_{fb} (V_{RHE}) is the potential of flat band; k_B is the Boltzmann constant (1.381×10^{-23} J K^{-1}) and T is the Kelvin temperature (298 K).

With the obtained N_d and V_{fb}, the W_{SCL} is calculated by the equation[5,12]:

$$W_{SCL} = \sqrt{\frac{2\varepsilon_0 \varepsilon_r (V - V_{fb})}{eN_d}} = \sqrt{\frac{2\varepsilon_0 \varepsilon_r V_{bi}}{eN_d}}$$

The E_{bi} and V_{bi} in the space charge layer are obtained by the equation with the obtained N_d and W_{SCL}[5]:

$$|E_{bi}| = \frac{eN_d}{\varepsilon_0 \varepsilon_r}|W_{SCL} - x|$$

$$|V_{bi}| = \frac{eN_d}{2\varepsilon_0 \varepsilon_r}(W_{SCL} - x)^2$$

where 'x' is the distance from the photoanode surface.

Calculation of the Debye screening length, and Thomas-Fermi screening length

According to the statistical models, the charge screening effect in a semiconductor can be described by Debye screening (Maxwell-Boltzmann statistics) or Thomas-Fermi screening (Fermi-Dirac statistics).

The λ_D is calculated by following equation[41,42]:

$$\lambda_D = \sqrt{\frac{\varepsilon_0 \varepsilon_r k_B T}{e^2 N_d}}$$

where ε_0 is the vacuum permittivity (8.854×10^{-12} F m^{-1}); ε_r is the relative permittivity of material; k_B is the Boltzmann constant (1.381×10^{-23} J K^{-1}); T is the Kelvin temperature (298 K); e is the electronic charge (1.602×10^{-19} C); and N_d (cm^{-3}) is the density of majority carrier.

The l_{TF} is calculated by following equation[43]:

$$l_{TF} = \sqrt{\frac{\varepsilon_0 \hbar^2 \pi^{\frac{4}{3}}}{3^{\frac{1}{3}} m_e e^2 N_d^{\frac{1}{3}}}}$$

where $\hbar$ is the reduced Planck constant (1.055×10^{-34} J·s), and m_e is the electron rest mass (9.109×10^{-31} kg).

For Fe_2O_3: ε_r is 32[31], and N_d is 1.2×10^{20} cm^{-3}, producing a λ_D ~ 0.62 nm and a l_{TF} ~ 0.17 nm.

For Sn-Fe_2O_3: ε_r is 32, and N_d is 2.6×10^{20} cm^{-3}, producing a λ_D ~ 0.42 nm and a l_{TF} ~ 0.15 nm.

For WO_3: ε_r is 20[44], and N_d is 2.9×10^{20} cm^{-3}, producing a λ_D ~ 1.8 nm and a l_{TF} ~ 0.26 nm.

For WO_3: ε_r is 20, and N_d is 3.5×10^{20} cm^{-3}, producing a λ_D ~ 0.62 nm and a l_{TF} ~ 0.18 nm.

For $BiVO_4$: ε_r is 68[45], and N_d is 4.3×10^{18} cm^{-3}, producing a λ_D ~ 4.7 nm and a l_{TF} ~ 0.29 nm.

For W-$BiVO_4$: ε_r is 68, and N_d is 8.4×10^{19} cm^{-3}, producing a λ_D ~ 1.1 nm and a l_{TF} ~ 0.18 nm.

For TiO_2: ε_r is 55[46], and N_d is 1.0×10^{19} cm^{-3}, producing a λ_D ~ 2.8 nm and a l_{TF} ~ 0.25 nm.

For Al-TiO_2: ε_r is 55, and N_d is 1.5×10^{19} cm^{-3}, producing a λ_D ~ 2.3 nm and a l_{TF} ~ 0.23 nm.

Data availability

Source Data file has been deposited in Figshare under accession code DOI link[47].

References

1. Corby, S., Rao, R. R., Steier, L. & Durrant, J. R. The kinetics of metal oxide photoanodes from charge generation to catalysis. *Nat. Rev. Mater.* **6**, 1136–1155 (2021).
2. Sivula, K. & van de Krol, R. Semiconducting materials for photoelectrochemical energy conversion. *Nat. Rev. Mater.* **1**, 15010 (2016).
3. Wang, Q., Pornrungroj, C., Linley, S. & Reisner, E. Strategies to improve light utilization in solar fuel synthesis. *Nat. Energy* **7**, 13–24 (2021).
4. Hemmerling, J. R., Mathur, A. & Linic, S. Design principles for efficient and stable water splitting photoelectrocatalysts. *Acc. Chem. Res.* **54**, 1992–2002 (2021).
5. Zhang, Z. & Yates, J. T. Jr. Band bending in semiconductors: chemical and physical consequences at surfaces and interfaces. *Chem. Rev.* **112**, 5520–5551 (2012).
6. Chen, R., Fan, F. & Li, C. Unraveling charge-separation mechanisms in photocatalyst particles by spatially resolved surface photovoltage techniques. *Angew. Chem. Int. Ed.* **61**, e202117567 (2022).
7. Zhu, J. et al. Direct imaging of highly anisotropic photogenerated charge separations on different facets of a single $BiVO_4$ photocatalyst. *Angew. Chem. Int. Ed.* **127**, 9239–9242 (2015).
8. Chen, R. et al. Spatiotemporal imaging of charge transfer in photocatalyst particles. *Nature* **610**, 296–301 (2022).
9. Barroso, M. et al. Dynamics of photogenerated holes in surface modified α-Fe_2O_3 photoanodes for solar water splitting. *Proc. Natl. Acad. Sci. USA.* **109**, 15640–15645 (2012).
10. Yao, T. et al. Manipulating the interfacial energetics of n-type silicon photoanode for efficient water oxidation. *J. Am. Chem. Soc.* **138**, 13664–13672 (2016).
11. Liu, G. et al. Enabling an integrated tantalum nitride photoanode to approach the theoretical photocurrent limit for solar water splitting. *Energy Environ. Sci.* **9**, 1327–1334 (2016).
12. Li, D. et al. Determining the transformation kinetics of water oxidation intermediates on hematite photoanode. *J. Phys. Chem. Lett.* **14**, 8069–8076 (2023).
13. Pendlebury, S. R. et al. Ultrafast charge carrier recombination and trapping in hematite photoanodes under applied bias. *J. Am. Chem. Soc.* **136**, 9854–9857 (2014).
14. Pastor, E. et al. In situ observation of picosecond polaron self-localisation in α-Fe_2O_3 photoelectrochemical cells. *Nat. Commun.* **10**, 3962 (2019).
15. Barroso, M., Pendlebury, S. R., Cowan, A. J. & Durrant, J. R. Charge carrier trapping, recombination and transfer in hematite (α-Fe_2O_3) water splitting photoanodes. *Chem. Sci.* **4**, 2724–2734 (2013).
16. Li, D. et al. Dynamic charge-collecting mechanisms of cobalt phosphate on hematite photoanodes studied by photoinduced absorption spectroscopy. *Chem. Sci.* **14**, 1861–1870 (2023).
17. Ruoko, T. P. et al. Subpicosecond to second time-scale charge carrier kinetics in hematite-titania nanocomposite photoanodes. *J. Phys. Chem. Lett.* **6**, 2859–2864 (2015).
18. Li, J. et al. Accelerated recombination reaction through interfacial Fe^{IV} = O accumulation on photoanode surfaces. *J. Am. Chem. Soc.* **147**, 21492–21500 (2025).
19. Pei, G. X., Wijten, J. H. J. & Weckhuysen, B. M. Probing the dynamics of photogenerated holes in doped hematite photoanodes for solar water splitting using transient absorption spectroscopy. *Phys. Chem. Chem. Phys.* **20**, 9806–9811 (2018).
20. Forster, M., Cheung, D. W. F., Gardner, A. M. & Cowan, A. J. Potential and pitfalls: on the use of transient absorption spectroscopy for in situ and operando studies of photoelectrodes. *J. Chem. Phys.* **153**, 150901 (2020).
21. Tian, C. M. et al. Electronic structure, optical properties, and photoelectrochemical activity of Sn-doped Fe_2O_3 thin films. *J. Phys. Chem. C* **124**, 12548–12558 (2020).
22. Zhou, Z., Long, R. & Prezhdo, O. V. Why silicon doping accelerates electron polaron diffusion in hematite. *J. Am. Chem. Soc.* **141**, 20222–20233 (2019).
23. Le Formal, F., Sivula, K. & Grätzel, M. The transient photocurrent and photovoltage behavior of a hematite photoanode under working conditions and the influence of surface treatments. *J. Phys. Chem. C* **116**, 26707–26720 (2012).
24. Delcompare-Rodriguez, P. A. & Seriani, N. Ultrathin space charge layer in hematite photoelectrodes: A theoretical investigation. *J. Chem. Phys.* **155**, 114701 (2021).
25. Naveas, N. et al. First-principles calculations of hematite (α-Fe_2O_3) by self-consistent DFT + U + V. *iScience* **26**, 106033 (2023).
26. Le Formal et al. Back electron-hole recombination in hematite photoanodes for water splitting. *J. Am. Chem. Soc.* **136**, 2564–2574 (2014).
27. Sachs, M. et al. Metal-centred states control carrier lifetimes in transition metal oxide photocatalysts. *Nat. Chem.* **17**, 1348–1355 (2025).
28. Sorenson, S. et al. Ultrafast carrier dynamics in hematite films: the role of photoexcited electrons in the transient optical response. *J. Phys. Chem. C* **118**, 23621–23626 (2014).
29. Liao, H. et al. Micro-heterogeneous annihilation dynamics of self-trapped excitons in hematite single crystals. *J. Phys. Chem. Lett.* **11**, 7867–7873 (2020).
30. Hayes, D. et al. Electronic and nuclear contributions to time-resolved optical and X-ray absorption spectra of hematite and insights into photoelectrochemical performance. *Energy Environ. Sci.* **9**, 3754–3769 (2016).
31. Zhang, H. et al. Gradient tantalum-doped hematite homojunction photoanode improves both photocurrents and turn-on voltage for solar water splitting. *Nat. Commun.* **11**, 4622 (2020).
32. Huang, Z. et al. In situ probe of photocarrier dynamics in water-splitting hematite (α-Fe_2O_3) electrodes. *Energy Environ. Sci.* **5**, 8923–8926 (2012).
33. Zhang, J. & Eslava, S. Understanding charge transfer, defects and surface states at hematite photoanodes. *Sustainable Energy Fuels* **3**, 1351–1364 (2019).
34. Wang, Z. et al. Synergetic effect of conjugated $Ni(OH)_2/IrO_2$ cocatalyst on titanium-doped hematite photoanode for solar water splitting. *J. Phys. Chem. C* **119**, 19607–19612 (2015).
35. Xu, C. et al. Parallel multi-stacked photoanodes of Sb-doped p–n homojunction hematite with near-theoretical solar conversion efficiency. *Nat. Commun.* **15**, 9712 (2024).
36. Liu, S. et al. Transition from sequential to concerted proton-coupled electron transfer of water oxidation on semiconductor photoanodes. *J. Am. Chem. Soc.* **145**, 23849–23858 (2023).
37. Maroo, S. et al. Electronic origin of reorganization energy in interfacial electron transfer. *Nature* **653**, 98–103 (2026).
38. Li, D. et al. Determining kinetics of H_2O_2 evolution from photoelectrochemical water oxidation. *Nat. Commun.* **16**, 7875 (2025).
39. Chen, R. et al. Linking the photoinduced surface potential difference to interfacial charge transfer in photoelectrocatalytic water oxidation. *J. Am. Chem. Soc.* **145**, 4667–4674 (2023).
40. Wan, T. H., Saccoccio, M., Chen, C. & Ciucci, F. Influence of the discretization methods on the distribution of relaxation times deconvolution: implementing radial basis functions with DRT tools. *Electrochim. Acta* **184**, 483–499 (2015).
41. Zhang, M. et al. Improved photoelectrochemical responses of Si and Ti codoped α-Fe_2O_3 photoanode films. *Appl. Phys. Lett.* **97**, 042105 (2010).
42. Liu, H. et al. One-step solvothermal formation of Pt nanoparticles decorated Pt^{2+}-doped α-Fe_2O_3 nanoplates with enhanced photocatalytic O_2 evolution. *ACS Catal* **9**, 1211–1219 (2019).

43. Scalfi, L. et al. A semiclassical Thomas-Fermi model to tune the metallicity of electrodes in molecular simulations. *J. Chem. Phys.* **153**, 174704 (2020).
44. Liu, X. et al. Oxygen-deficient WO_{3-x} nanoplate array film photoanode for efficient photoelectrocatalytic water decontamination. *Chem. Eng. J.* **381**, 12274 (2020).
45. Zhong, D. K., Choi, S. & Gamelin, D. R. Near-complete suppression of surface recombination in solar photoelectrolysis by "Co-Pi" catalyst-modified W:$BiVO_4$. *J. Am. Chem. Soc.* **133**, 18370–18377 (2011).
46. Salvador, P. Hole diffusion length inn-TiO_2 single crystals and sintered electrodes: photoelectrochemical determination and comparative analysis. *J. Appl. Phys.* **55**, 2977–2985 (1984).
47. Li, D. et al. Disentangling the effect of space and electric field on photoelectrochemical water splitting. *Figshare*. https://doi.org/10.6084/m9.figshare.33075917 (2026).

Acknowledgements

Prof. Qinlin Guo (Institute of Physics) is kindly acknowledged for his assistance in XPS measurement.

Author contributions

D.L., L.L., X.W. and Y.W. conceived and designed the experiments. D.L. carried out the experiments, analysed data and wrote the manuscript. L.Z. and X.W. tested and analysed μs-s TA spectra. L.W. retested in-situ fs-ns TA spectra. Y.X., H.M., Y.H., J.Z., Z.W. and H.C. assisted TA spectra tests and analysed the data. L.L., X.W. and Y.W. supervised the experiments and contributed to the data analysis. All authors have given approval to the final version of the manuscript.

Funding

We acknowledge financial support from the National Key Research and Development Program of China (2023YFA1507001), the CAS project for Young Scientists and Basic Research (YSBR-007), and the National Natural Science Foundation of China (92577208, 22222308, 22502231). This work was supported by Synergetic Extreme Condition User Facility (SECUF) in Beijing.

Competing interests

The authors declare no competing interests.

Additional information

Supplementary information The online version contains supplementary material available at https://doi.org/10.1038/s41467-026-77786-5.

Correspondence and requests for materials should be addressed to Li Liu, Xiuli Wang or Yuxiang Weng.

Peer review information *Nature Communications* thanks the anonymous reviewer(s) for their contribution to the peer review of this work. A peer review file is available.